

Automated Tire Visual Inspection Based on Low Rank Matrix Recovery

Guangxu Li

Qingdao University of Science and Technology

Zhouzhou Zheng

Qingdao University of Science and Technology

Yuyi Shao

Qingdao University of Science and Technology

Jinyue Shen

Qingdao University of Science and Technology

Yan Zhang (✉ zy@qust.edu.cn)

Qingdao University of Science and Technology

Research Article

Keywords: visual inspection, low rank matrix recovery, weight matrix

Posted Date: November 20th, 2020

DOI: <https://doi.org/10.21203/rs.3.rs-109309/v1>

License:  This work is licensed under a Creative Commons Attribution 4.0 International License.

[Read Full License](#)

Automated Tire Visual Inspection Based on Low Rank Matrix Recovery

Guangxu Li¹, Zhouzhou Zheng¹, Yuyi Shao¹, Jinyue Shen¹, Yan Zhang^{1,*}

¹College of Mechanical and Electrical Engineering, Qingdao University of Science and Technology, Qingdao 266061, China

Corresponding author: Yan Zhang (e-mail: zy@qust.edu.cn)

Abstract

Visual inspection is a challenging and widely employed process in industries. In this work, an automated tire visual inspection system is proposed based on low rank matrix recovery. Deep Network is employed to perform texture segmentation which benefits low rank decomposition in both quality and computational efficiency. We propose a dual optimization method to improve convergence speed and matrix sparsity by incorporating the improvement of the soft-threshold shrinkage operator by the weight matrix M . We investigated how incremental multiplier affects the decomposition accuracy and the convergence speed of the algorithm. On this basis, image blocks were decomposed into low-rank matrix and sparse matrix in which defects were separated. Comparative experiments have been performed on our dataset. Experimental results validate the theoretical analysis. The method is promising in false alarm, robustness and running time based on multi-core processor distributed computing. It can be extended to other real-time industrial applications.

1. Introduction

Tires, as one of the most important parts of cars that withstand the friction and weight, are crucial for driving safety. Due to the use of unclean raw materials and inaccurate production equipment in the tire manufacturing process, defects such as foreign matter incorporation, air bubbles, cracking of the texture, etc. occur in the tires. Accordingly, in tire manufacturing industry, nondestructive testing via automated visual inspection system based on machine vision is an indispensable stage in the production processes. However, many tire manufacturers still use naked-eye detection in tire radiographic images obtained by the vision system. This inspection has a low detection efficiency, low accuracy and is sensitive to the tiredness of the inspectors. Thus, inspection has become one of the technical bottlenecks of intelligent manufacturing. The tire industry is experiencing an urgent need of automated, non-destructive visual inspection systems.

To date, a variety of automated visual inspection methods were investigated and proposed for different industrial applications, such as fabrics, weld IC, rail surface and strip steel [1-3] etc. However, few studies have investigated the automated tire defect visual inspection problem. In recent years, the problem has been attracting significant attention in academic and industry.

Normally, the problems for automated tire inspection fall into the following categories including statistical approach [4], spectral approach [5-6], learning approach [7-9], structural approach [10], and other hybrid methods [11]. In [4], Zhao and Qin proposed a detection method using local inverse difference moment features and received good performance except that only foreign object defects were tested. Guo et al. [10] proposed a tire defect detection method based on weighted texture difference. Feature similarity was used to capture the texture distortion of each pixel by weighted averaging the dissimilarity between the pixel and its neighborhoods. The method can automatically detect texture and foreign body defects in tread and sidewall with a detection accuracy of 85% and 93.3% respectively. Due to its complexity, the cost in computational time of the method is high. Li [12] proposed a radial tire defect detection in radiographic images based on fuzzy edge detection method. In [13], a dictionary representation-based tire defect detection algorithm was proposed. The distribution of representation coefficients was used as a discrimination criterion to detect defects.

In previous research, researchers have studied tire defect detection problem utilizing wavelet multiscale analysis [5], edge detection [6], total variation image decomposition [11] and deep learning [7-9] in tire radiographic or laser shearography images. Wavelet multi-scale analysis based method [5] can segment defective edge and normal textures by computing the optimal scale and threshold parameters and reached a satisfactory detection accuracy for foreign object defects. In [6], the authors combine curvelet transform and Canny edge operator for tire inspection on laser shearography images. To eliminate the influence of anisotropic multi-texture in tire radiographic images, in [11] a total variation based method was proposed to decompose tire radiographic images into texture and cartoon components such that foreign bodies and bubble defects can be detected easily. However, these methods tend to be sensitive to the choice of selected parameters for different types of tires and detection applications.

Deep learning techniques have demonstrated remarkable effectiveness in solving image classification, text recognition etc. and have been utilized in visual inspection systems recently [14]. A concise semantic segmentation network (Concise-SSN) is proposed [7], which realizes defect segmentation including Belt-Joint-Open and Foreign-Matter. In [8], tire defect classification and end-to-end defect detection problem was investigated based on convolutional neural networks (CNNs). Deep learning models rely highly on a large number of samples to obtain high precision. He Kaiming *et al.* [15] promoted the Faster R-CNN network model towards

real-time object detection with Region Proposal Networks, which greatly accelerated the efficiency of deep learning object detection networks and was widely used in object detection. Al Arif *et al.* [16] Proposed a fully automatic U-Net-based framework for segmenting the cervical spine in X-ray images and received satisfactory segmentation accuracy. It is undeniable that deep learning methods for the purpose of object detection or image segmentation inevitably have limitations. Designing a suitable DNN architecture for a given problem continues to be a challenging task. To design a deep learning model with empirically selected hyper-parameters from scratch for a specific application can be a very complicated and tedious process that is prohibitively expensive in terms of computational resources and time. It is also worth noting that deep network approaches could be lack of necessary flexibility and robustness for industrial applications.

In many tire manufacturing companies, tire visual inspection tasks are still carried out by human operators [5]. There are two main reasons for this. Firstly, unlike inspection problems for fabrics, paper and rail surface etc. in which the background textures are usually unified, tire defect detection is particularly challenging due to the large number of defect categories and complex anisotropic textures. Tire defects, like small crack or bubble that hidden in tread can hardly be detected using existing techniques. Compared with other visual inspection applications listed above, a fast, simple, robust and automated tire visual inspection is remaining a challenging research topic.

Low rank matrix recovery (LRMR) has been proved to have good application prospects in image decomposition and target detection. Yang *et al.* [17] proposed a block-based RPCA robust moving object detection method in which inexact Lagrangian augmented multipliers (IALM) method was used to obtain satisfying foreground detection. Cao *et al.* [18] used the optimal threshold method and low rank representation to achieve automatic segmentation of white blood cells. Peng Li *et al.* [19] proposed a fabric defect detection method based on improved low rank representation (LRR) algorithm. The method is simple, accurate and with less restrictive conditions.

Tire radiographic image consist of a basic pattern. The structural information of the image matrix has strong correlation such that they can be mapped into a lower dimensional linear subspace which can be expressed by fewer linear independent vectors. In addition, tire defects, foreign matters for example, are mostly small objects that are mis-incorporated into the rubber. Such objects occupy a small portion of the image matrix, and appear as black bars in tire radiographic images. They have weak correlation, deviate from the low-rank subspace, and would be decomposed into the sparse matrix image as noise. Texture defects mainly include texture breakage, texture spacing, texture bending, etc., which are significantly different from normal tire texture in terms of direction, spacing and shape. As a result, tire radiographic images are of low rank and therefore can be decomposed by LRMR into low rank background matrices and sparse matrices, wherein the sparse matrices include weakly correlated components in the original matrix such as noise and possible defects. Compared with hand-crafted approaches that rely on a selection of pre-defined features and parameters, LRMR based method can perform robust decomposition and detection.

When performing low rank decomposition on tire X-ray image, the algorithm converges very slowly, about 260s per image. On the other hand, noises in the sparse matrix also make it difficult to detect defects. In this context and in order to alleviate the above mentioned difficulties, in this work we use semantic texture segmentation to improve the low rank characteristics of tire images, and improve the representative Inexact Augmented Lagrange Multiplier (IALM) algorithm [20] in LRMR problem in convergence speed and matrix sparsity.

We make three specific contributions in this paper. Firstly, we advocate the use of an improved soft threshold operator method over the conventional IALM method for noise suppression. We argue that noise suppression in the sparse matrix can be obtained by applying the approach to the objective as a whole. Secondly, we demonstrate that dual optimization in convergence speed and matrix sparsity can be solved efficiently and explicitly, outperforming that using conventional algorithms, by incorporating the improvement of the soft-threshold shrinkage operator by the weight matrix M . Finally, we present a semantic texture segmentation model based on SegNet [21] for image rank reduction. As a result, we demonstrate an improvement in the decomposition quality and detection accuracy of the proposed method. The running time of the model can satisfy real world applications.

This paper is organized as follows. The theoretical foundations of the low rank matrix recovery and the proposed scheme are presented in Section 2. In Section 3, experiments are described with the automated tire visual inspection system. Experimental results are presented and discussed in Section 4 including a comparison results of state-of-the-art methods. Finally, conclusions are delivered in Section 5.

2. Theory and algorithm

2.1. Matrix low rank decomposition

Given a matrix with low rank characteristics and some severely damaged elements, LRMR refers to the problem of how to restore the original matrix by automatically identifying the damaged elements. At the same time, the severely damaged elements only account for a small part of the original matrix, that is, the noise is sparse but the value can be arbitrary. The low rank matrix restoration assumes that the image background is located in a low-dimensional subspace, approximated by a low rank matrix. The significant target deviates from the low-rank subspace as noise and is represented by a sparse matrix. Hence, the task of recovering low-rank and sparse components [22], which is a non-deterministic polynomial (NP-Hard) problem, can be accurately accomplished in the probabilistic sense via solving the following nuclear-norm and l_1 -norm-involved convex relaxation problem.

As a generalization of signal sparse representation in compressed sensing, different models have been developed to perform LRMR in the literature. It is mainly composed of three types of models: Robust Principal Components Analysis (RPCA) [23], Matrix Completion (MC) [24] and Low-Rank Representation (LRR) [25]. Among them RPCA represents the data matrix as the sum of the low rank matrix and the sparse noise matrix, and then recovers the low rank matrix by solving the kernel norm optimization problem. The model has been widely studied and applied in numerous applications, such as video surveillance, image alignment, graph clustering, covariance estimation, latent semantic index and low rank texture etc. The matrix low rank decomposition model can be defined as

$$D = A + E \quad (1)$$

where D denotes a corrupted high-dimensional matrix, $D \in R^{m \times n}$, A is a low rank matrix representing the image background and, E is a sparse matrix representing the corrupted portion or a noise portion. Equation (1) is a two-objective optimization problem. After introducing the regularization parameter λ , it can be transformed into the following optimization problem

$$\min \text{rank}(A) + \lambda \|E\|_0, \quad \text{subject to } D = A + E. \quad (2)$$

where $\|E\|_0$ represents the zero-order norm of the matrix E , that is the number of non-zero elements in the matrix E . λ is a regularization parameter, usually $\lambda = 1/\sqrt{\max(m, n)}$, in which m and n are the number of rows and columns of the matrix D . The above optimization problem is a non-deterministic polynomial (NP-Hard) problem. Since the nuclear norm of a matrix is the envelop of the matrix rank, the l_1 -norm of the matrix is a convex hull of the zero-order norm. Equation (2) is generally relaxed into a convex optimization problem.

$$\min_{A, E} \|A\|_* + \lambda \|E\|_1, \quad \text{subject to } D = A + E \quad (3)$$

where $\|A\|_*$ represents the kernel norm of A , that is the sum of the singular values of A . $\|\cdot\|_1$ represents the l_1 -norm. Due to convex optimization by principal component tracking can accurately recover low rank and sparse components in the matrix, this optimization is referred to as Robust PCA (RPCA). This principal component pursuit (PCP) approach [26] shown in (3) recovers the low-rank and the sparse matrices.

2.2. Weighted contraction IALM algorithm

The matrix low rank sparse decomposition process involves a large number of singular values which result in a large amount of data computation and a slow convergence speed. In real world applications, a typical tire radiographic image for example, is a large digital matrix, such that acceleration strategies are essential to ensure low computational complexity and acceptable accuracy at the same time.

To solve these problems, researchers have recently proposed a large variety of algorithms [27] based on the PCP model, such as Robust Subspace Learning (RSL), Stable Principal Component Pursuit (SPCP), Augmented Lagrange Multiplier (ALM), Inexact Augmented Lagrange Multiplier (IALM), Accelerated Proximal Gradient (APG), Alternating Direction Method (ADM), and Templates for First-Order Conic Solvers (TFOCS), Bayesian Framework (BRPCA) etc.

IT (Iterative thresholding) algorithm [28] is effective for l_1 -norm minimization problem, but convergence is very slow. In IT algorithm, the RPCA problem (3) is converted to

$$\min_{A, E} \|A\|_* + \lambda \|E\|_1 + \frac{1}{2\tau} \|A\|_F^2 + \frac{1}{2\tau} \|E\|_F^2 \quad \text{subject to } A + E = D \quad (4)$$

By introducing the Lagrange multiplier Y to eliminate the equality constraint, we get the Lagrangian function of (4) as

$$L(L, S, Y) = \|A\|_* + \lambda \|E\|_1 + \frac{1}{2\tau} \|A\|_F^2 + \frac{1}{2\tau} \|E\|_F^2 + \langle Y, D - A - E \rangle \quad (5)$$

The IT algorithm is simple and provably correct; however, it requires a large number of iterations to converge and, it is difficult to select step size for acceleration. This limits its applicability. The introduction of the augmented Lagrangian multiplier method [20] can solve this problem.

$$L(X, Y, \mu) = f(X) + \langle Y, h(X) \rangle + \frac{\mu}{2} \|h(X)\|_F^2 \quad (6)$$

where μ is a positive scalar. When $\{\mu_k\}$ is an increasing sequence and both f and h are continuous differentiable functions, the Lagrangian multiplier Y_k converges to the optimal solution in a Q-linear manner when $\{\mu_k\}$ is bounded. Moreover, the optimal step size to update Y_k is proven to be the chosen penalty parameter μ_k , making algorithm parameter adjustment easier than the IT algorithm. The advantage of the ALM method is that even if μ_k does not need to be close to infinity, it can converge to the optimal solution.

$$L(A, E, Y, \mu) = \|A\|_* + \lambda \|E\|_1 + \langle Y, D - A - E \rangle + \frac{\mu}{2} \|D - A - E\|_F^2 \quad (7)$$

Equation (7) is refer to as exact ALM (EALM) method. In fact, it is not the larger the μ_k , the faster the EALM algorithm converges. When μ_k is larger, the EALM algorithm calculates an increase number of SVDs, and the convergence of the sub-problem $(A_{k+1}^*, E_{k+1}^*) = \min_{A, E} L(A, E, Y_k, \mu_k)$ will be slower.

Unlike EALM, the IALM algorithm does not need to find the exact solution of the above sub-problem exactly. Alternately, as in (8) and (9), updating A_k and E_k once when solving this sub-problem is sufficient for A_k and E_k to meet the optimal convergence condition of the PRCA problem [20].

$$A_{k+1} = \arg \min_A L(A, E_{k+1}, Y_k, \mu_k) = D_{\mu_k^{-1}}(D - E_{k+1} + \mu_k^{-1}Y_k) \quad (8)$$

$$E_{k+1} = \arg \min_A L(A_{k+1}, E, Y_k, \mu_k) = S_{\lambda/\mu_k}(D - A_{k+1} + \mu_k^{-1}Y_k) \quad (9)$$

where $S_\varepsilon[x]$ is the soft-threshold contraction operator to modify each element in the matrix. It was introduced by the IT algorithm and is used in the IALM algorithm.

$$S_\varepsilon[x_{ij}] = \begin{cases} x_{ij} - \varepsilon, & \text{if } x_{ij} > \varepsilon, \\ x_{ij} + \varepsilon, & \text{if } x_{ij} < -\varepsilon, \\ 0, & \text{otherwise,} \end{cases} \quad (10)$$

where $x_{ij} \in \mathbb{R}$ and $\varepsilon > 0$.

It is worth noting that the soft threshold operator used in IALM is not efficient to handle the sparse matrix E_k . After the algorithm converges, noise remains in E_k , which will affect subsequent defect detection processing. Therefore, sparse matrix noise suppression is an important task in this work. To do that, assuming that possible defective parts are represented with noise in the sparse matrix E_k , we mainly explore the problem of sparse matrix noise suppression. An improved IALM algorithm named Weighted contraction IALM (WIALM) is introduced by introducing a new soft threshold operator

$$TS_\varepsilon[x_{ij}] = \begin{cases} x - \varepsilon \cdot M_{ij}, & \text{if } x > \varepsilon, \\ x + \varepsilon \cdot M_{ij}, & \text{if } x < -\varepsilon, \\ 0, & \text{otherwise,} \end{cases} \quad (11)$$

where the matrix $M \in R^{m \times n}$ is a weight matrix, which has the same dimension as A_k and E_k . It is used to reduce noise in E_k by suppressing defect-free textures.

The matrix A_k relies on the singular value decomposition of the matrix, and uses the main singular values and their corresponding eigenvectors as the principal component subspace of the matrix. For low rank tire images, the principal component subspace contains background texture information with significant correlation, and shields the noise interference of the sparse subspace. The construction of the matrix M is derived from the A_k since the information of defect-free texture is included in the low-rank matrix of each tire image block

$$M = \frac{S_\alpha[|A_k|]}{\alpha} \quad (12)$$

where $|A_k|$ is the absolute value of A_k ,

$$\alpha = \|A_k\|_{inf}/m \quad (13)$$

where

$$S_\alpha[x_{ij}] = \begin{cases} x_{ij} = \alpha, & \text{if } x_{ij} < \alpha \\ x_{ij}, & \text{otherwise} \end{cases} \quad (14)$$

where m is the horizontal dimension of principal component matrix A_k of tire radiographic image block, $\|A_k\|_{inf}$ represents the maximum value of the sum of the absolute values of the elements of each row of the matrix A_k . Because the texture direction of the tire X-ray image is anisotropic and periodic, the texture gap can be extracted according to the threshold parameter α set by the gray value interval of the principal component matrix $A_k \in R^{m \times n}$. The texture gap of the tire image contains a large amount of sparse noise. By increasing the corresponding weights of these elements, their gray values are accelerated to shrink in each iteration, and they are suppressed in E_k . As shown in Fig. 1, the weighted part of the weight matrix M is displayed in the original image in red, and it is obvious that the weight distribution does not include the defect region. This shows that the improved soft threshold operator proposed for the purpose of performing sparse matrix noise suppression has no interference with defect detection.

The weighted contraction IALM used in the tire defect inspection application is as follows.

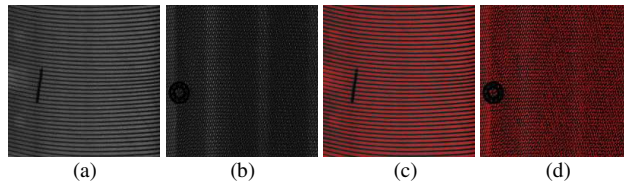


Figure 1. (a), (b) test images; (c), (d) Distribution of weighting matrix M for the corresponding test images.

WIALM algorithm used in tire defect inspection

Input: $D \in R^{m \times n}$, λ , ρ , τ .

- 1: **Initialize** $Y_0 = D/J(D)$, $E_0 = 0$, $\mu_0 > 0$, $k = 0$.
- 2: **while** not converged **do**
- 3: $(U, S, V) = \text{svd}(D - E_k + \mu_k^{-1}Y_k)$,
- 4: $A_{k+1} = US_{\mu_k^{-1}}[S]V^T$,
- 5: $M = S_\alpha(|A_{k+1}|)/\alpha$,
- 6: $E_{k+1} = T\mathcal{S}_{\lambda\mu_k^{-1}}[D - A_{k+1} + \mu_k^{-1}Y_k]$,
- 7: $Y_{k+1} = Y_k + \mu_k(D - A_{k+1} - E_{k+1})$,
- 8: **Update** $\mu_{k+1} = \mu_k \times \rho$
- 9: $k=k+1$.
- 10: **end while**

Output: (A_k, E_k)

2.3. Optimization of algorithmic parameters

In the above algorithm, the convergence of the low-rank matrix image is obtained by the iterative Lagrangian multiplier algorithm. Each iterative process needs to perform a singular value decomposition. The low-rank characteristic of the tire radiographic image is obvious, and the redundant calculation will unnecessarily increase computing time. Considering the characteristics of tire radiographic imaging, it is essential to optimize the parameters of the proposed algorithm to meet the requirements of practical application and increase the efficiency and precision of tire inspection.

In this algorithm, the parameters involved are regularization parameter λ , initial positive scalar μ_0 , incremental multiplier ρ and iterative stop parameter τ . Wherein, the regularization parameter λ can be determined by the input dimensions $\lambda = 1/\sqrt{\max(m, n)}$ as in [29]. In the IALM algorithm [20], the iteration termination condition is defined as $\frac{\|D - A_k - E_k\|_{Fro}}{\|D\|_{Fro}} < \tau$, where $\|D\|_{Fro} = \sqrt{\sum D^2(i, j)}$. The iteration stop parameter τ determines whether the algorithm converges, which is the condition for the algorithm to stop iteration. If the parameter τ is too large, it will reduce the number of iterations, thereby increasing the segmentation error. Instead, it will increase redundant calculation time. In this work, according to experience, τ is determined as 10^{-7} .

Initially positive scalar $\mu_0 = \frac{1.5}{\|D\|_2}$, where $\|\cdot\|_2$ represents the maximum singular value of the matrix D . The incremental multiplier ρ is multiplied by μ_k to update the positive scalar μ_{k+1} . In [30], Lin et al. prove that when μ_k is non-decreasing and $\sum_{k=1}^{+\infty} \mu_k^{-1} = +\infty$, (A_k, E_k) approaches to an optimal solution (A^*, E^*) to the RPCA problem. In this work, we fasten the update speed by adjusting the incremental multiplier under $\rho > 1$ condition. The selection of the incremental multiplier ρ of the penalty parameter $\{\mu_k\}$ will affect the number of algorithm iterations and the running time. Optimal ρ should be selected.

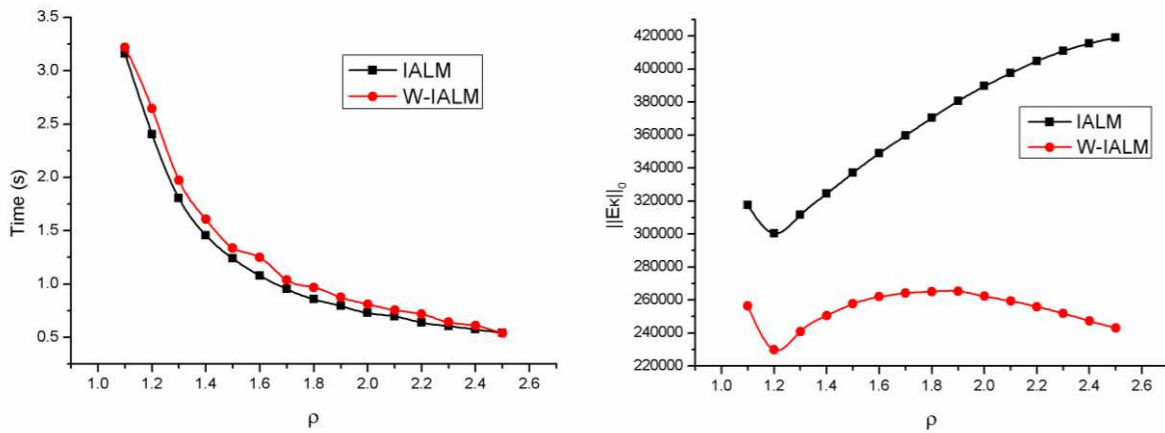


Figure 2. Performance change curve of IALM algorithm and W-IALM algorithm related to incremental multiplier ρ

In order to realize on-line detection, the time complexity of the IALM algorithm needs to be further optimized. In Fig. 2, obtained the relationship between the incremental multiplier parameter ρ and iteration numbers, algorithm convergence time and $\|E_k\|_0$ through experiments.

As is shown in Fig. 2, as a parameter of μ_k , as the incremental multiplier ρ increases the iteration numbers and algorithm convergence time decreases exponentially. When ρ is larger, the reduction in computational complexity begins to slow down. It is

worth noting that the value of $\|E_k\|_0$ will increase at the same time, which means that the amount of noise in the sparse matrix will increase, and noise points will stick to form many connected regions, which will be difficult to distinguish from defects, and the detection effect will become worse. For the same image, in our improved algorithm, the value of $\|E_k\|_0$ decreases with increasing ρ . This shows that the improvement of the soft-threshold shrinkage operator by the weight matrix M is effective. The improved algorithm can achieve dual optimization in convergence speed and sparse matrix quality. In this work, we set $\rho=2.4\sim 2.6$ for μ_k .

2.4. Flowchart of the proposed scheme

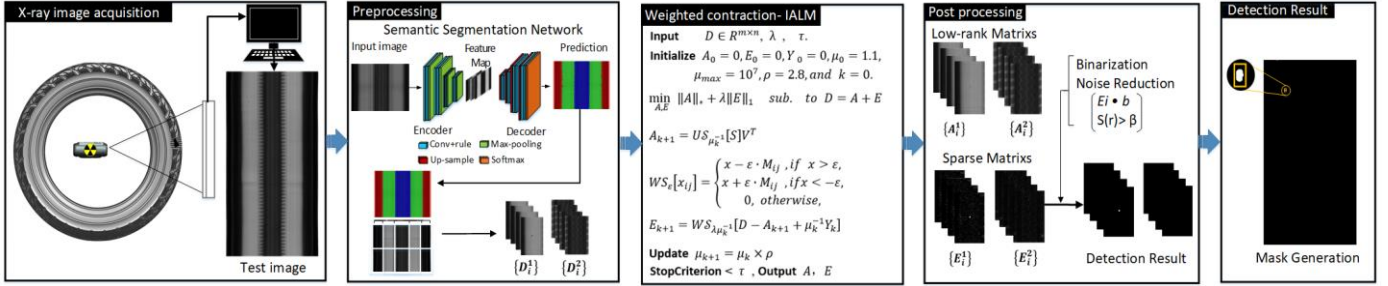


Figure 3. A flowchart of the proposed scheme.

In the following, as shown in Fig. 3, we briefly describe the proposed automated tire visual inspection scheme.

1) Image acquisition

In image acquisition stage, test images are captured by tire X-ray inspection machine for a variety category of tires. Both defective and defect-free ones are collected.

2) Preprocessing

The preprocessing stage is composed by three main operations including down-sampling, texture segmentation and image blocking. Firstly, image down-sampling is implemented to reduce computational complexity and improve efficiency. Secondly, semantic texture segmentation is performed for image rank reduction. Thirdly, test images are divided into blocks based on texture segmentation results. The advantages of the preprocessing are twofold. The complexity of problem space is further reduced such that the running time can be reduced using parallel computing for image blocks. Moreover, texture segmentation would enhance the linear correlation of the image blocks, which theoretically helps to achieve better low rank decomposition results. The texture segmentation algorithm is introduced in detail in the following section.

3) Image decomposition

We next apply the proposed WIALM algorithm to the image blocks to show how well the algorithm works with real world data. The choice of incremental multiplier parameter ρ will be discussed via experiments in detail. The foreground consisting of noise and potential defects is modeled as a sparse matrix E_i , and the background consisting of normal tire textures is modeled as a low rank matrix A_i . We ensure decomposition efficiency by limiting the number of iterations using an improved soft-threshold contraction operator to limit iterations the ALM and SVD algorithm can run for.

4) Post processing

Weakly correlated information of anisotropic textures in test images results in additional noise in sparse matrices when performing decomposition and thus would affect defect detection accuracy. Therefore, noise reduction processing is necessary for defect isolation. Mathematical morphology based noise reduction is applied to the E_i matrices. Masks are generated by combining the E_i matrices and up sampled to original dimensions. Two adjacent defects in different image blocks are merged. Finally, the defect masks with pixel-level defect amount, shapes, sizes and locations are outputted.

3. Experimental results

In this section, the performance of the proposed automated tire online visual inspection algorithm is evaluated. The experiments have been conducted with Intel(R) Core (TM) i7-8700 CPU @ 3.20GHz 3.19GHz processor and 8.0 GB RAM.

3.1. Dataset description

A dataset composed of 1000 tire radiographic images was collected by X-ray inspection machine from a real-world tire production line. Different types of tire radiographic images with different defects were collected. The test images are 8-bit greyscale images

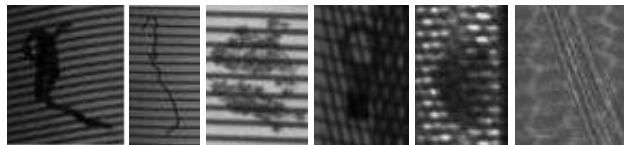


Figure 4. Tire defect samples of the dataset in the experiments.

with dimension of 11400×2469 pixels. The defects are of 2 typical categories, namely foreign matter defect (including Belt-Foreign-Matter, Sidewall-Foreign-Matter) and texture defect (including Belt-Joint-Open, Bulk-Sidewall etc.). Fig. 4 shows sample synopses of the experimental dataset.

3.2. Texture semantic segmentation

In the test image of 11400×2469 pixels obtained in the tire factory, the low-rank matrix decomposition will be a matrix iterative operation with more than 2.8×10^7 elements. The running time is very long. It is about 260 seconds on this experimental platform, which cannot meet the requirements of industrial online Testing requirements. On the other hand, in the sparse matrix obtained by low-rank matrix decomposition of the entire test image, as shown in Fig. 5, obvious noise will appear at the boundary of different textures, which will affect the accuracy of defect detection.

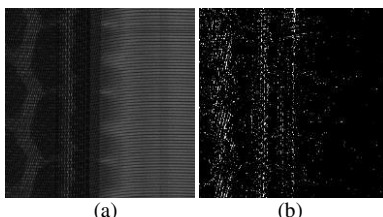


Figure 5. (a) Sample tire X-ray image with different textures, (b) Sparse matrix of (a) decomposed by IALM algorithm.

The WIALM algorithm is an iterative solution method, and GPU parallel computing cannot be used. Experiments show that as the matrix size decreases, the convergence time of the RPCA algorithm will be greatly shortened. Therefore, dividing the image into blocks and then distributing the image blocks will save the total calculation time [31]. The texture segmentation of tire X-ray images will further simplify the problem space and improve the vector correlation of each image block matrix, which will help improve the accuracy of the WIALM algorithm.

Strong anisotropy of different types of tread patterns make it infeasible to apply conventional segmentation methods. Recently, semantic segmentation networks have shown satisfactory pixel-wise results without artificial designed features [32]. Therefore, we train a semantic tire texture segmentation network using transfer learning on our dataset using SegNet model [21]. Considering the memory requirements when training the network, original test images are first down sampled by 4, then they are divided into image blocks of 360×618 pixels. The dataset consists of 1000 images in which 600 of them are the training set, 200 of them are the validation set and the rest are the test set. As shown in Fig. 6, semantic segmentation results indicate that the mean segmentation accuracy and Intersection over Union (IoU) of the model can reach 91.17% and 82.62% on our dataset. The accuracy can satisfy segmentation requirement.

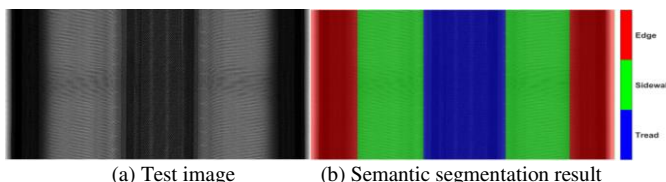


Figure 6. Tire X-ray image semantic segmentation result.

3.3. Tire inspection and post processing

After texture semantic segmentation, we apply the proposed WIALM algorithm to perform low rank decomposition on the image blocks. **Fig. 2** shows the performances of conventional IALM with default parameters, conventional IALM with optimal parameter ρ , and the proposed WIALM respectively. The number of iterations of SVD, $\text{Rank}(A_k)$, $\|E_k\|_0$, and convergence time are taken into consideration in which $\|E_k\|_0$ represents the zero-order norm of E_k .

Method	SVD	$\text{Rank}(A_k)$	$\ E_k\ _0$	Time(s)
IALM	38	179	1316574	6.795
OP-IALM	21	172	1494090	2.805
Our method	16	307	734536	2.703

It can be seen from Table 1 that for tread test images of size 1000 by 307, compared with conventional IALM, with optimal parameter ρ it can reduce the number of iterations of SVD and can greatly reduce convergence time. However, parameter optimization has little effect on the low-rank matrix A_k and $\|E_k\|_0$. Our proposed WIALM algorithm can not only greatly reduce the number of iterations of SVD, convergence time, but also can reduce the number of non-zero elements in the sparse matrix E_k ,

namely noise and defects, from 1316574 and 14940490 to 734536 on average. At the same time, the $\text{Rank}(A_k)$ is improved from 179 and 172 to 307 using our method on average.

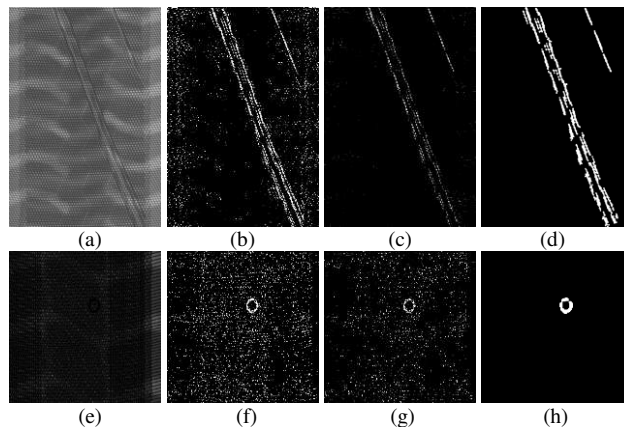


Figure 7. Experimental results of the proposed method. (a) and (e): Test images; (b) and (f): Binarization of sparse matrices using IALM; (c) and (g): Binarization of sparse matrices using our WIALM; (d) and (h): Final detection results using our method.

Fig. 7 shows experimental results of the proposed method. The defective test images in Fig. 7 (a) and (e) were cropped and enlarged for better visual effects. Fig. 7 (b), (f) show binarization of sparse matrices using IALM algorithm; (c) and (g) show binarization of sparse matrices using our WIALM algorithm in which background noise are greatly reduced compared with (b), (f), which verified the results in Table 1.

To further eliminate background noise, post processing operations using mathematical morphological are applied based on the statistics of the gray value of defects in the sparse matrix. Fig. 7 (d), (h) show final detection results using our method. Defective regions can be successfully detected at a satisfactory defection rate. The final results provide complete and clear defect masks in a noise-free background which are sufficient for industrial applications.

4. Discussion

In this section, the performance, accuracy, and efficiency of the proposed method are tested and comparative experiments are performed on our experimental dataset. Experimental results are discussed to indicate the advantages and disadvantages of the proposed algorithm.

Table 2 Experimental results of the proposed method

	Texture defect	Foreign matter	False alarm	Number of samples
Sidewall	96.0%	95.7%	2.4%	500
Tread	95.4%	95.0%	3.8%	500

Table 2 shows tire visual inspection results on our dataset. The detection accuracy of the proposed method is higher than 95%, a false alarm lower than 4%, and is robust to different tire patterns. The accuracy for sidewall is higher than that of the tread area, and the false alarm is lower than that of the tread.

Benefitting from the pre-processing operations and image block distributed computing, the running time of the algorithm is greatly shortened. Our final implementation took, on average, 9.76 seconds to process the complete tire radiographic image of 11400×2469 pixels using the MATLAB 2019b using distributed computing in a Windows 10 64-bit system with 6-core Intel CPU device. The running time is shorter than that of workers' naked-eye detection adopted by many manufacturing enterprises (15

seconds per tire). Thus, the proposed scheme can be applied to online inspection.

To validate the effectiveness of the proposed algorithm, comparative experiments are conducted on the same dataset. We experiment on weighted-texture-dissimilarity (WTD) [10], U-Net [33], Deeplabv3+ [34] and Faster R-CNN [15]. In WTD, feature similarity is used to capture the texture distortion of each pixel by weighted averaging the dissimilarity between the pixel and its neighborhoods for defect detection. In U-Net, features are extracted and fused by trained convolutional neural networks. In Deeplabv3+, depthwise separable convolution and atrous spatial pyramid pooling(ASPP) module are applied to expand receptive field for getting richer feature information. Faster RCNN network performs well in many applications for object detection problems. As shown in Table 3, the proposed method outperforms the state-of-the-art methods in overall inspection accuracy, false alarm and non-detection rates on our dataset. The overall successful detection accuracy for tread and sidewall reached 95.2% and 95.8% respectively.

Table 3 Comparative experimental results

Methods	False Alarm	Tread	Sidewall
WTD [10]	4.5%	85.0%	93.0%
U-Net [32]	9.8%	84.0%	90.0%
Deeplabv3+ [34]	5.8%	89.1%	90.8%
Faster R-CNN[15]	12.8%	82.0%	88.2%
Our method	3.1%	95.2%	95.8%

As shown in Fig. 8, the WTD method is susceptible to interference from complex anisotropic textures. This can cause imperfections or discontinuities in defective areas. The results using U-net introduce non-defective noises. Due to insufficient segmentation of Deeplebv3+, it cannot provide accurate defect edge information. Faster R-CNN method can only detect and locate defects in bounding boxes. The detection accuracy of this method is highly dependent on training sample capacity and training parameters. Experimental results indicate that the proposed method can perform satisfactory inspection for online application.

Comparative result with state-of-the-art methods						
Test image	Ground Truth	WTD[10]	U-Net[33]	Deeplabv3+[34]	Faster RCNN[15]	Our Method

Figure 8. Comparative experimental results with the state-of-the-art methods.

Non-detection or poorly performing test samples in the dataset were analyzed. As shown in Fig. 9, there are challenges in detecting defects like mild bubbles, uneven distribution of cords and extremely tiny foreign matter etc. It is worth noting that these samples can hardly be detected even for experienced human workers in naked-eye inspection.

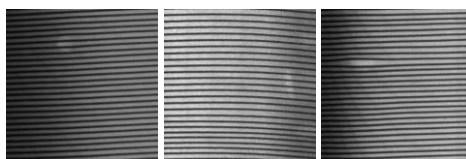


Figure 9. Non-detection or poorly performing samples in the test dataset.

5. Conclusions

In this research, we detailed an automated tire visual inspection system based on low rank matrix recovery for online application. We demonstrated that tire radiographic images have low rank property. Tire defect detection can be regarded as a problem of recovering the low-rank and sparse components of a given matrix in which defective parts are represented together with noise as the sparse matrix. Based on the naive model, we improved the efficiency of the algorithm by optimizing incremental multiplier parameter. Semantic texture segmentation was applied for rank and running time reduction to make it be suitable for online inspection. Comparative experiments were conducted to validate the efficiency of the method with the state-of-the-art methods.

Experimental results show that the method outperforms state-of-the-art methods in overall detection accuracy, defect integrity, false alarm and robustness on our dataset. The computational efficiency of the proposed scheme is suitable for online inspection. The method can be extended to other visual inspection industrial applications.

References

- [1] J. Sun, C. Li, et al., "An Effective Method of Weld Defect Detection and Classification Based on Machine Vision," *IEEE Trans. Ind. Inform.*, vol. 15, pp. 6322-6333, 2019.
- [2] J. Zhang, H. Wang, Y. Tian, et al. "An accurate fuzzy measure-based detection method for various types of defects on strip steel surfaces," *Comput. Ind.*, vol.122, pp. 103231,2020.
- [3] J. Zhu, Q. Min, et al., "Probability of Detection or Eddy Current Pulsed Thermography of Angular Defect Quantification," *IEEE Trans. Ind. Inform.*, vol. 14, no. 12, pp. 5658-5666, 2018.
- [4] G. Zhao, and S. Qin, "High-Precision Detection of Defects of Tire Texture Through X-ray Imaging Based on Local Inverse Difference Moment Features," *Sensors*, vol. 18, no. 8, pp. 2524, 2018.
- [5] Y. Zhang, D. Lefebvre and Q. Li, "Automatic Detection of Defects in Tire Radiographic Images," *IEEE Trans Autom. Sci. Eng.*, vol. 14, no. 3, pp. 1378-1386, July 2017.
- [6] Y. Zhang, T. Li and Q. Li, "Defect detection for tire laser shearography image using curvelet transform based edge detector," *Opt. Laser Technol.*, vol. 7, pp. 64-71, Apr. 2013.
- [7] Z. Zheng, S. Zhang, B. Yu, Q. Li and Y. Zhang, "Defect Inspection in Tire Radiographic Image Using Concise Semantic Segmentation," in *IEEE Access*, vol. 8, pp. 112674-112687, 2020.
- [8] Y. Zhang, XH. Cui, Y. Liu and Y. Bin, "Tire Defects Classification Using Convolution Architecture for Fast Feature Embedding," *Int. J. Comput. Int. Sys.*, vol. 11, pp. 1056-1066, 2018.
- [9] R. Wang, Q. Guo, S. Lu and C. Zhang, "Tire Defect Detection Using Fully Convolutional Network," *IEEE Access*, vol. 7, pp. 43502-43510, 2019.
- [10] Q. Guo, C. Zhang, et al., "Defect Detection in Tire X-Ray Images Using Weighted Texture Dissimilarity," *J. Sensors*, vol. 2016, pp.1-12, 2016.
- [11] Y. Zhang, T. Li and Q.L. Li, "Detection of Foreign Bodies and Bubble Defects in Tire Radiography Images Based on Total Variation and Edge Detection," *Chin. Phys. Lett.*, vol. 8, pp. 256-307, Aug. 2013.
- [12] F. Y. Li, "The study of an improved fuzzy edge detection algorithm in the radial tire quality detection," *Advanced Materials Research*, vol. 317-319, pp. 968-971, 2011.
- [13] Y. Xiang, C. Zhang and Q. Guo, "A Dictionary-based Method for Tire Defect Detection," in *Proc. IEEE Int. Conf. Infor. and Automat.*, pp. 519-523, 2014.
- [14] R. Ren, T. Hung and K. C. Tan, "A Generic Deep-Learning-Based Approach for Automated Surface Inspection," *IEEE Trans. Cybernetics*, vol. 48, no. 3, pp. 929-940, March 2018.
- [15] Shaoqing Ren, Kaiming He, Ross Girshick and Jian Sun, "Faster R-CNN: Towards Real-Time Object Detection with Region Proposal Networks," *IEEE T. Pattern Anal.*, vol. 39, no. 6, pp. 1137-1149, 2017.
- [16] S M Masudur Rahman Al Arif, Karen Knapp, Greg Slabaugh, "Fully automatic cervical vertebrae segmentation framework for X-ray images," *Comput. Meth. Prog. Bio.*, vol. 157, pp. 95-111, 2018.
- [17] B. Yang, L. Zhou, "Robust foreground detection using block-based RPCA," *Optik*, vol. 126, pp. 4586-4590, 2015.
- [18] F. Cao, M. Cai, J. Chu, et al., "A novel segmentation algorithm for nucleus in white blood cells based on low-rank representation," *Neural Comput. Appl.*, vol.28, no.1, pp.503-511, May.2016.
- [19] P. Li, J. Liang, et al., "Textile fabric defect detection based on low-rank representation," *Multimed. Tools Appl.*, vol. 78, pp. 99-124, 2019.
- [20] Z. Lin, M. Chen, et al., "The Augmented Lagrange Multiplier Method for Exact Recovery of Corrupted Low-Rank Matrices," arXiv:1009.5055, 2013.
- [21] V. Badrinarayanan, A. Kendall et al., "SegNet: A Deep Convolutional Encoder-Decoder Architecture for Image Segmentation," *IEEE Trans. Pattern Anal.*, vol 39, no.12, pp. 2481-2495, 2017.
- [22] M .Tao, X .Yuan. "Recovering low-rank and sparse components of matrices from incomplete and noisy observations". *SIAM Journal on Optimization*, , vol.21,no.1, pp.57-81,2011.
- [23] E. J. Candes, X. Li, Y. MA et al., "Robust principal component analysis?" *J. ACM*, vol. 58, pp. 1-37, 2011.
- [24] E. J. Candes, T. Tao, "The Power of Convex Relaxation: Near-Optimal Matrix Completion," *IEEE Trans. Inform. Theory*, vol. 56, no. 5, pp. 2053-2080, May 2010.
- [25] G. Liu, Z. Lin et al., "Robust recovery of subspace structures by low-rank representation," *IEEE Trans. Pattern Anal.*, vol. 35, pp.171-184,2013.
- [26] J. Wright, Y. Peng, Y. Ma, A. Ganesh, S. Rao, "Robust principal component analysis: Exact recovery of corrupted low-rank matrices by convex optimization," *Neural Information Processing Systems*, NIPS 2009.
- [27] T. Bouwmans, E. H. Zahzah, "Robust PCA via Principal Component Pursuit: A review for a comparative evaluation in video surveillance," *Comput. Vis. Image Und.*, vol. 122, pp. 22-34, 2014. DOI: 10.1016/j.cviu.2013.11.009.
- [28] J. Eckstein, D. Bertsekas, "On the Douglas-Rachford Splitting Method and the Proximal Point Algorithm for Maximal Monotone Operators," *Math. Program.*, vol. 55, pp.293-318, 1992.
- [29] Z. Zhou, X. Li, J. Wright, E. Candes, Y. Ma, "Stable principal component pursuit," *IEEE ISIT Proceedings*, pp. 1518-1522, 2010.
- [30] Lin, Z., Ganesh, A., Wright, J., Wu, L., Chen, M., Ma, Y. "Fast convex optimization algorithms for exact recovery of a corrupted low-rank matrix," *SIAM J. Optimization*
- [31] G. Tang, A. Nehorai, "Robust principal component analysis based on low-rank and block-sparse matrix decomposition," *CISS*, 2011.
- [32] A. Garcia-Garcia, S. Orts-Escolano, et al., "A survey on deep learning techniques for image and video semantic segmentation," *Appl. Soft Comput.*, vol. 70, pp. 41-65, 2018.
- [33] O. Ronneberger, P. Fischer, T. Brox, "U-Net: Convolutional Networks for Biomedical Image Segmentation," *LNCS*, 9351, pp. 234-241, 2015.

[34] L.C. Chen, Y. Zhu, G. Papandreou, *et al.* “Encoder-decoder with atrous separable convolution for semantic image segmentation” ECCV, pp. 801-818, 2018.

Acknowledgements

This work was supported by the Natural Science Foundation of Shandong Province No. ZR2019MEE066 and partly by No. ZR2018MC007.

Author contributions statement

G.L. processed the image and calculated the data calculation and made the tables and the figures and wrote the manuscript. Z.Z. gave advice about image processing. Y.S. and J.S. collected the data. Y. Z. presented the concept of the research and supervised this study.

Competing interests

The authors declare no competing interests.

Additional information

Correspondence and requests for materials should be addressed to Y.Z.

Reprints and permissions information is available at www.nature.com/reprints.

Publisher’s note Springer Nature remains neutral with regard to jurisdictional claims in published maps and institutional affiliations.

Figures

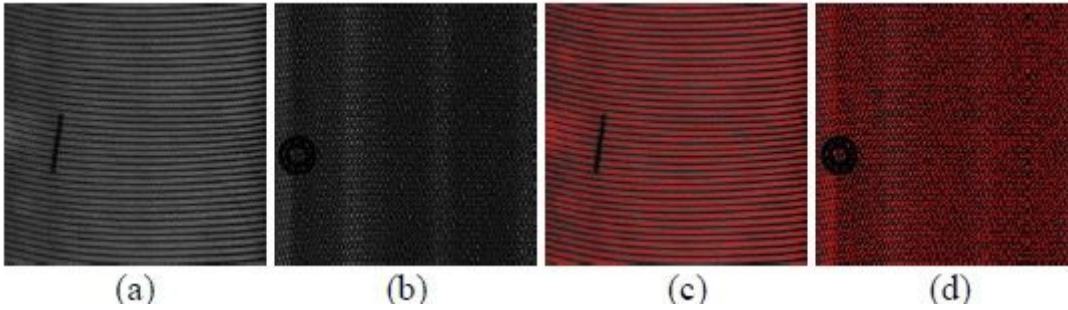


Figure 1

(a), (b) test images; (c), (d) Distribution of weighting matrix M for the corresponding test images.

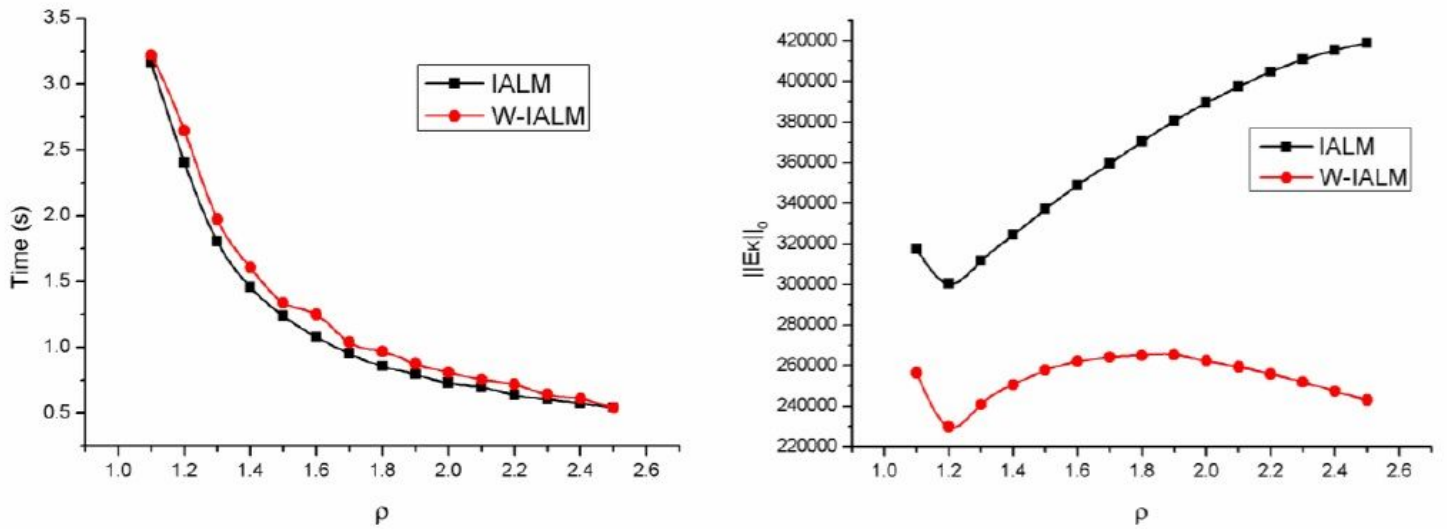


Figure 2

Performance change curve of IALM algorithm and W-IALM algorithm related to incremental multiplier ρ

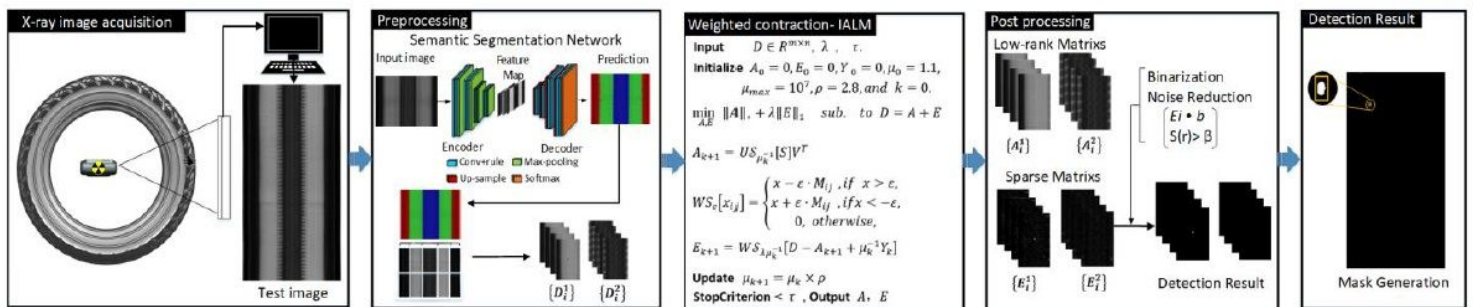


Figure 3

A flowchart of the proposed scheme.

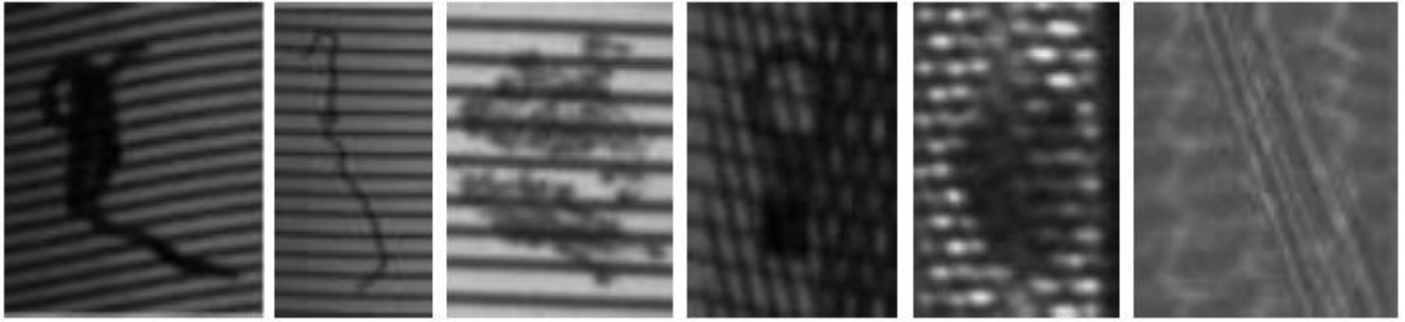


Figure 4

Tire defect samples of the dataset in the experiments.

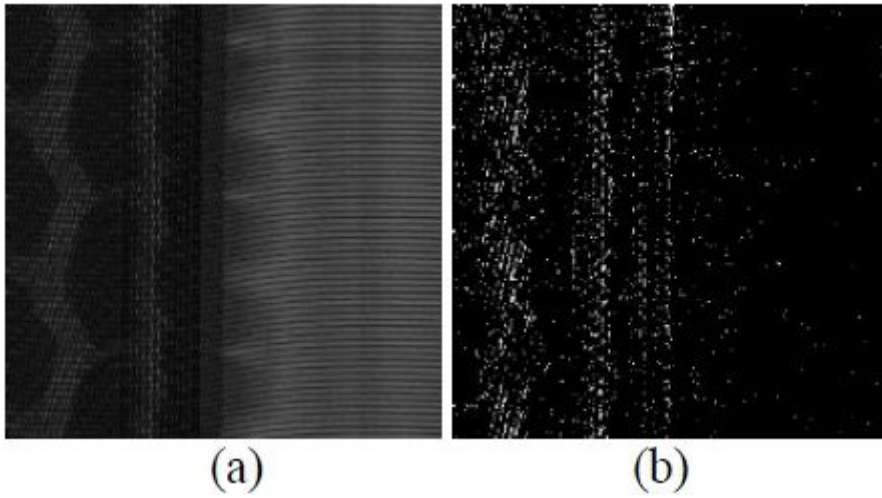


Figure 5

(a) Sample tire X-ray image with different textures, (b) Sparse matrix of (a) decomposed by IALM algorithm.

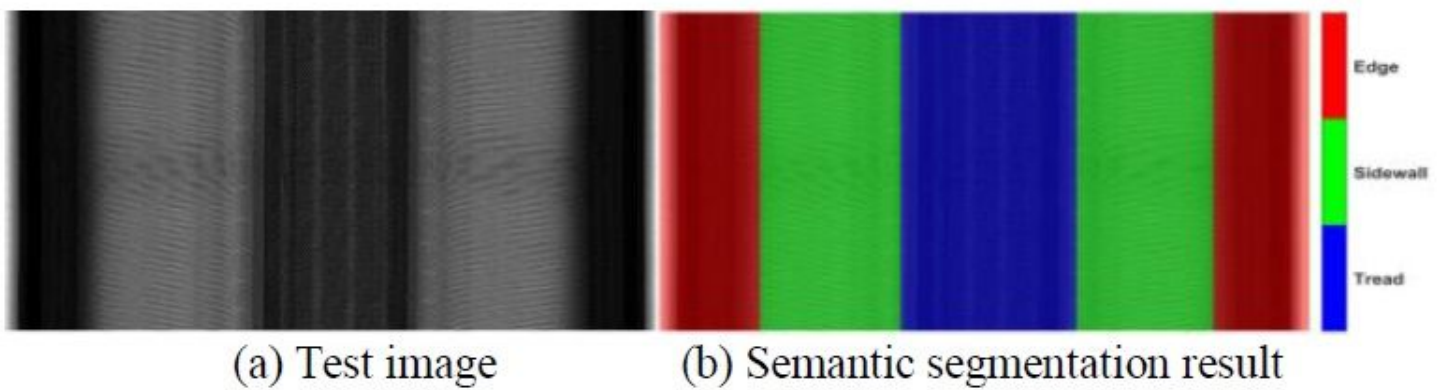


Figure 6

Tire X-ray image semantic segmentation result.

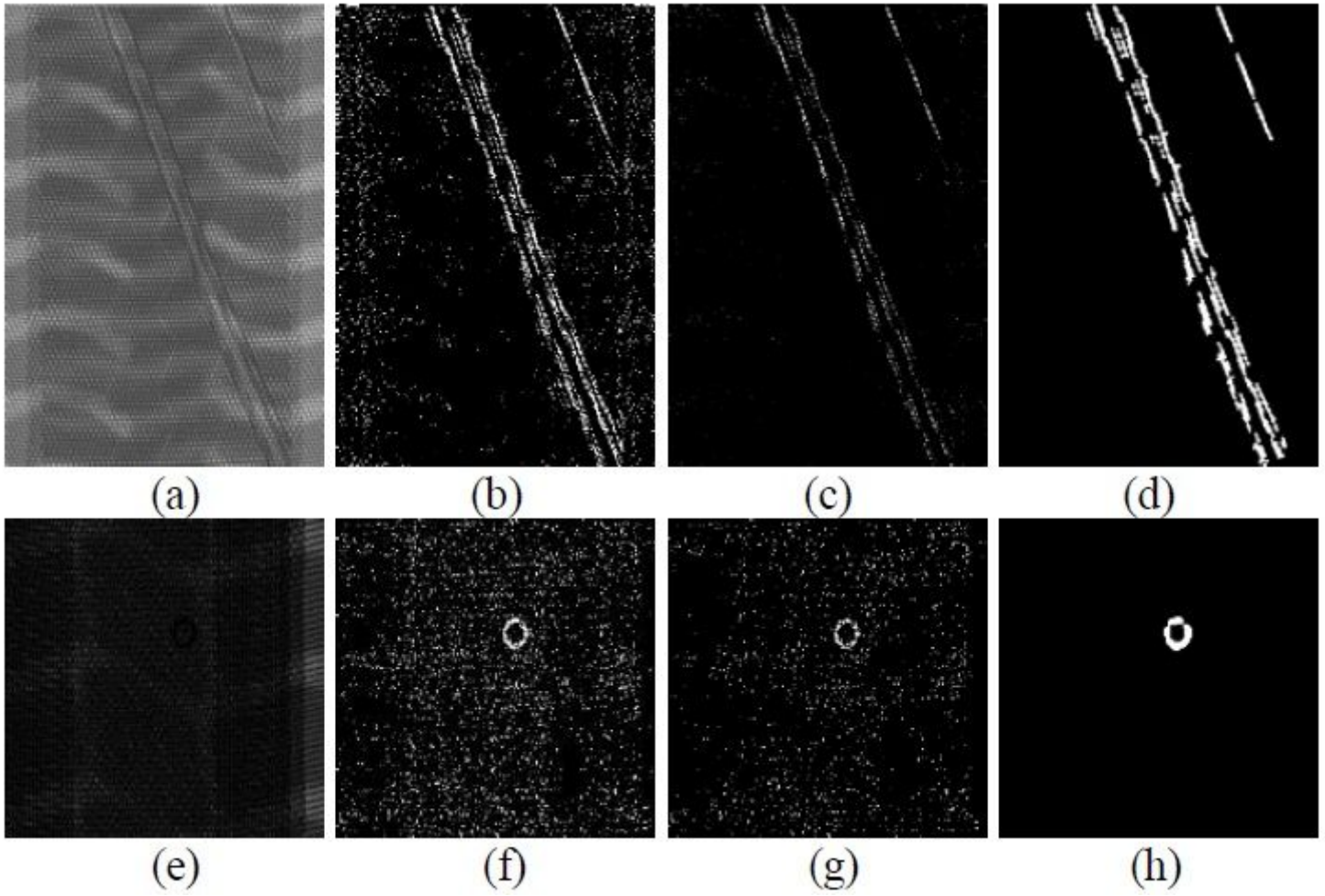


Figure 7

Experimental results of the proposed method. (a) and (e): Test images; (b) and (f): Binarization of sparse matrices using IALM; (c) and (g): Binarization of sparse matrices using our WIALM; (d) and (h): Final detection results using our method.

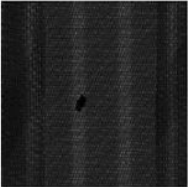
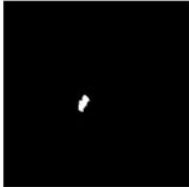
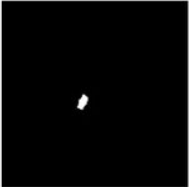
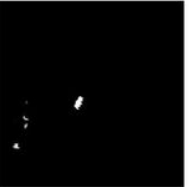
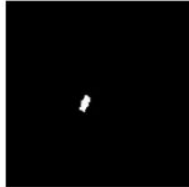
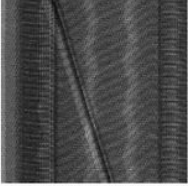
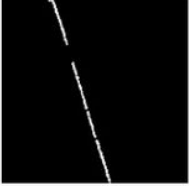
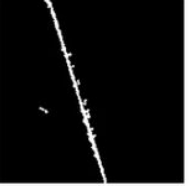
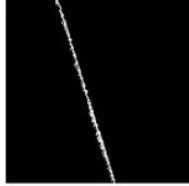
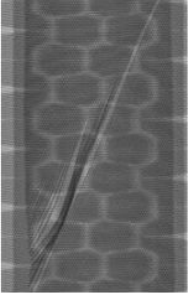
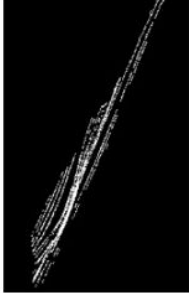
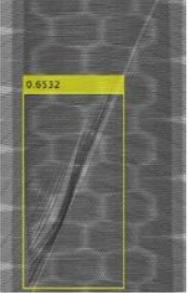
Comparative result with state-of-the-art methods						
Test image	Ground Truth	WTD[10]	U-Net[33]	Deeplabv3+[34]	Faster RCNN[15]	Our Method
						
						
						

Figure 8

Comparative experimental results with the state-of-the-art methods.

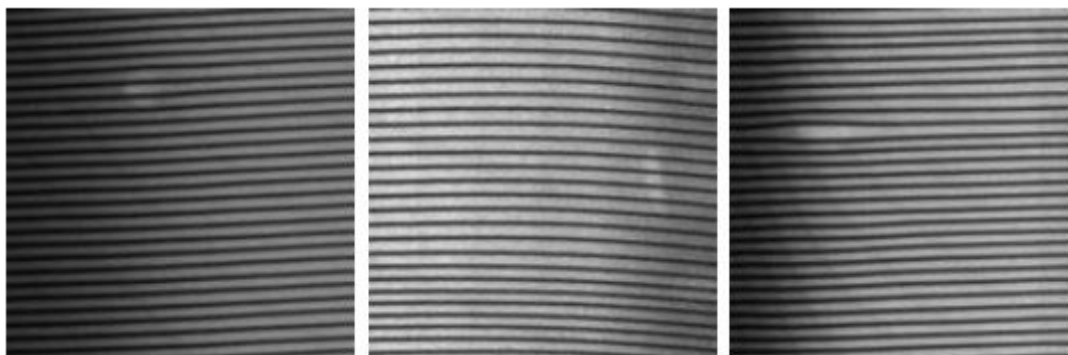


Figure 9

Non-detection or poorly performing samples in the test dataset.